

Available online at www.sciencedirect.com

ScienceDirect
Journal of Hydrodynamics

www.sciencedirect.com/science/journal/10016058

2010,22(6):745-752

DOI: 10.1016/S1001-6058(09)60112-8

WAVE-BODY INTERACTIONS FOR A SURFACE-PIERCING BODY IN WATER OF FINITE DEPTH^{*}

LI Yong, LIN Mian

Institute of Mechanics, Chinese Academy of Sciences, Beijing 100190, China, E-mail: liyong@imech.ac.cn

(Received June 17, 2010, Revised August 30, 2010)

Abstract: Nonlinear wave-body interactions for a stationary surface-piercing body in water of finite depth with flat and sloping bottoms are simulated in a two-dimensional numerical wave tank, which is constructed mainly based on the spatially averaged Navier-Stokes equations with the $k-\varepsilon$ model for simulating the turbulence. The equations are discretized based on the finite volume method and the scheme of the pressure implicit splitting of operators is employed to solve the Navier-Stokes equations. By using the force time histories, the mean and higher-harmonic force components are calculated. The computational results are shown to be in good agreement with experimental and numerical results of other researchers. Then, the horizontal force, the vertical force and the moment on the surface-piercing body under nonlinear regular waves with flat and sloping bottoms are obtained. The results indicate that the bottom topographies have a significant influence on the wave loads on the surface-piercing body.

Key words: wave-body interaction, surface-piercing body, numerical wave tank, finite water depth

1. Introduction

Many types of surface-piercing structures, such as jacket platforms and man-made islands, have been used in coastal engineering in the offshore oil and gas development. Usually the structures are subjected to strong nonlinear water wave impacts and are precarious under the extreme ocean situations. Therefore, it is important to investigate the wave forces on surface-piercing structures in water of finite depth.

There are many studies of the interactions between the water waves and structures of various immersed types, for example, the fully submerged structures^[1-3], vertical bodies reposed on seabed^[4-6] and the surface-piercing bodies^[7-10]. Among them, the problems of surface-piercing bodies have attracted much attention recently. Tanizawa and Minami^[7] developed a two dimensional numerical wave tank to

simulate the radiation and diffraction of a single surface-piercing body. Bai et al.^[8] investigated the nonlinear hydrodynamic forces on a surface-piercing body of arbitrary shape in three dimensions by a time domain second-order method. Koo and Kim^[9] considered the single and double bodies based on potential theory and Boundary Element Method (BEM). Wang et al.^[10] developed a three dimensional time-domain coupled numerical model to obtain the nonlinear wave forces acting on a box-shaped body. In these studies, the effects of the water depth are neglected.

In the present article, the wave forces and the rotational moments are investigated for a fixed structure under the finite water depth condition. First, a 2-D numerical wave tank is built and verified. The simulated results are compared with the experimental results of Nojiri and Murayama^[11], the analytical solution of Maruo^[12] and the numerical results of Koo and Kim^[9]. Second, the nonlinear wave-body interactions with a flat bottom are simulated in this tank. The mean wave force, the harmonic force components and the rotational moments on the body are calculated and the results are compared with those under the condition of deep water. Finally, the wave loads on a fixed body with sloping topography is

^{*} Project supported by the National Natural Science Foundation of China (Grant No. 40776057), the Knowledge Innovation Program of Chinese Academy of Sciences (Grant Nos. KJCX2-YW-L07, KZCX2-YW-212-2).

Biography: LI Yong (1978-), Male, Ph. D.

Corresponding author: LIN Mian,

E-mail: linmian@imech.ac.cn

studied.

2. Mathematical formulation

2.1 Governing equations

The governing equations are the Reynolds averaged Navier-Stokes equations

$$\frac{\partial \rho}{\partial t} + \frac{\partial}{\partial x_j} (\rho u_j) = 0 \quad (1)$$

$$\frac{\partial}{\partial t} (\rho u_i) + \frac{\partial}{\partial x_j} (\rho u_j u_i) = -\frac{\partial p}{\partial x_i} + \frac{\partial}{\partial x_j} \left[\mu_e \left(\frac{\partial u_j}{\partial x_i} + \frac{\partial u_i}{\partial x_j} \right) \right] - D_i u_i + \rho g_i \quad (2)$$

where $x_j (j=1,2,3)$ represents the coordinate components, u_j is the fluid velocity, p is the pressure, ρ is the density, g is the acceleration of gravity, and D_i is the damping coefficient and the damping term $D_i u_i$ is added to the momentum equation directly. $\mu_e = \mu + \mu_f$, where μ is the fluid viscosity, $\mu = 1.002 \times 10^{-6} \text{ m}^2 \text{ s}$, μ_f is the turbulent eddy viscosity, $\mu_f = C_\mu \rho k^2 / \varepsilon$. k is the turbulent kinetic energy, and ε is the turbulent energy dissipation rate. The $k-\varepsilon$ two-equation model is adopted to estimate the turbulence.

$$\frac{\partial}{\partial t} (\rho k) + \frac{\partial}{\partial x_j} (\rho u_j k) = \frac{\partial}{\partial x_j} \left[\left(\mu + \frac{\mu_f}{\delta_k} \right) \frac{\partial k}{\partial x_j} \right] + P_k - \rho \varepsilon \quad (3)$$

$$\frac{\partial}{\partial t} (\rho \varepsilon) + \frac{\partial}{\partial x_j} (\rho u_j \varepsilon) = \frac{\partial}{\partial x_j} \left[\left(\mu + \frac{\mu_f}{\delta_\varepsilon} \right) \frac{\partial \varepsilon}{\partial x_j} \right] + C_1 P_k \frac{\varepsilon}{k} - \rho_f C_2 \frac{\varepsilon^2}{k} \quad (4)$$

$$P_k = \mu_f \left(\frac{\partial u_i}{\partial x_j} + \frac{\partial u_j}{\partial x_i} \right) \frac{\partial u_i}{\partial x_j} \quad (5)$$

where δ_k and δ_ε are the turbulent Schmidt

numbers. The constants in Eqs.(3)-(5) take the following values: $C_\mu = 0.09$, $C_1 = 1.44$, $C_2 = 1.92$, $\delta_k = 1.0$ and $\delta_\varepsilon = 1.33$.

In order to capture the water-air free surface, an Eulerian method named the Volume Of Fluid (VOF) method is adopted. The equation for the volume fraction is

$$\frac{\partial \alpha}{\partial t} + \frac{\partial}{\partial x_j} (u_j \alpha) = 0 \quad (6)$$

where α is the volume fraction of water and $1-\alpha$ represents the volume fraction of air. The volume fraction of each liquid is used as the weighting factor to get the mixture properties, such as density and viscosity, i.e.,

$$\rho = \alpha \rho_w + (1-\alpha) \rho_a \quad (7)$$

where ρ_w and ρ_a represent the density of water and air, respectively.

2.2 Numerical scheme

The equations are discretized based on the Finite Volume Method (FVM). In order to guarantee the computational precision, the central difference scheme with second-order accuracy and the Quadratic Upwind Interpolation of Convective Kinematics (QUICK) scheme with third-order accuracy are employed to represent the diffusion term and convection term, respectively. The Preconditioning Conjugate Gradient (PCG) method is employed for solving the algebraic equations. For solving the Navier-Stokes equation of incompressible fluid flow, one will encounter a problem of the pressure-velocity coupling. Here, the Pressure Implicit Splitting of Operators (PISO) scheme is employed to treat the coupling. k and ε equations are coupled in the scheme and solved by a segregated approach. For the sake of computational stability, the Courant number is used to obtain the time step at every beginning of the calculation cycle ($C_n = 0.1$ for wave cases), defined as

$$C_n = \frac{u_i \Delta t}{\Delta x_i} \quad (8)$$

where Δt is the time step and Δx_i represents the mesh size.

When the solution in the fluid domain is obtained, the time history of the wave force on the bodies can be obtained by integrating the pressure and the viscous force. The flow chart for the simulation process is plotted in Fig.1, where "tnow" is the current time in calculation and "tend" is the total calculation time.

For a free surface simulation, generally, the divergence is an issue, because of the sharp interface between water and air. In this work, a Compressive Interface Capturing Scheme for Arbitrary Meshes (CICSAM) is used to capture the fluid interfaces with meshes of arbitrary topology. Details about the CICSAM can be found in Ubbink and Issa^[13].

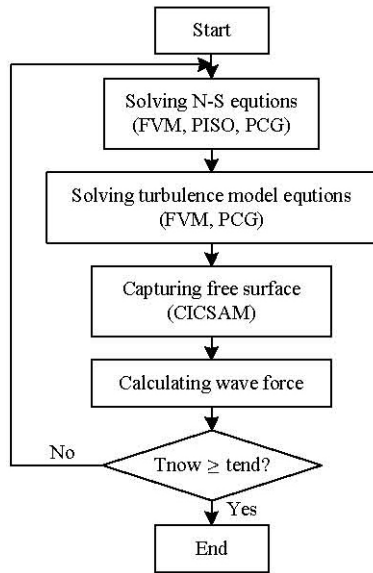


Fig.1 Computation flow chart

The entire computational domain with the bottom topography is shown in Fig.2 and there are basically five types of boundary associated with the governing equation: inlet, outlet, structure wall, bed, and atmosphere.

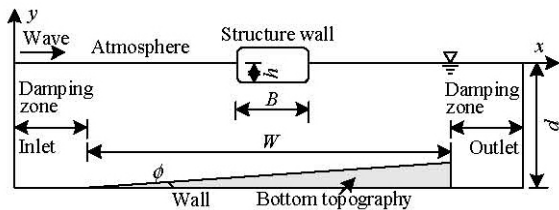


Fig.2 Sketch of the fluid domain with the bottom topography

Boundary conditions associated with regular waves are prescribed along the inlet of the computational domain. The pressure and the turbulence quantities including k and ε are set to be of zero normal gradient and the velocity vector is specified by Stokes and Cnoidal regular waves. The theoretical velocity of second-order Stokes regular waves can be expressed by

$$u_x^m = \frac{agA}{\omega} \frac{\text{cha}(z+d)}{\text{ch}ad} \cos(ax - \omega t) +$$

$$\frac{3\omega a A^2}{8} \frac{\text{ch}2a(z+d)}{\text{sh}^4 ad} \cos 2(ax - \omega t) \quad (9)$$

$$u_y^m = \frac{agA}{\omega} \frac{\text{sha}(z+d)}{\text{ch}ad} \sin(ax - \omega t) +$$

$$\frac{3\omega a A^2}{8} \frac{\text{sh}2a(z+d)}{\text{sh}^4 ad} \cos 2(ax - \omega t) \quad (10)$$

where A , ω , a and d are the wave amplitude, frequency, wave number, and water depth, respectively. x is the distance from the origin to the wave making point.

At the outlet, the pressure and the turbulence quantities are also specified as of zero normal gradients and the velocity is specified by Sommerfeld radiation condition, expressed by

$$\frac{\partial u}{\partial x} + \frac{1}{c} \frac{\partial u}{\partial t} = 0 \quad (11)$$

where c is the wave propagation velocity at the end point of the damping zone.

At the surfaces of the structure, no slip wall boundary condition is used. The velocity vector at the bed is set to be zero and the zero normal gradient condition is chosen for other quantities.

For the atmosphere boundary, the total pressure is set to zero and k and ε are set with zero normal gradient. The bottom boundary of the domain is the bed. No slip wall boundary condition and the wall function are used. The wall function can be summarized as follows^[14]

$$l_m = \beta_0 L \left[\exp\left(\frac{\kappa u}{u_*}\right) - 1 \right] \quad (12)$$

$$k = \frac{u_*^2}{\sqrt{C_\mu}} \quad (13)$$

$$\varepsilon = \frac{u_*^3}{l_m} \quad (14)$$

where l_m represents the mixing length, β_0 is a constant, $\beta_0 = 0.005$, κ is the Karman constant, $\kappa = 0.4$, u_* is the friction velocity, L is the characteristic length, which is the distance of the

centre of the near-wall grid to the bottom wall.

2.3 Numerical implementation

The programming is based on the open source computational fluid dynamics code named Open Field Operation And Manipulation (OpenFOAM), of the version 1.5, which can be downloaded freely through the internet (OpenCFD 2008). OpenFOAM provides a fundamental platform to write new solvers for different problems and the tensorial approach and the object oriented techniques are used. Xu^[15] studied the numerical wave tank with OpenFOAM, but with the damping zone being ignored.

In the present work, the solution for the computational domain is carried out by the adoption of the turbulence solver for incompressible two-phase flow. Based on Eqs.(12)-(14), the default wall function in OpenFOAM is modified. The inflow boundary and two damping zones are added to the original OpenFOAM solver. As for the inlet location, according to Eq.(9) and Eq.(10), a new wave making boundary named “wavetimevarying” is programmed with C++ language. Correspondingly, in order to absorb the wave energy reflection from the end-wall and the re-reflection from the input boundary, artificial damping zones are allocated at the two ends of the domain. In this paper, for the right end damping zone, the damping term $D_i u_i$ is added to the momentum equation of OpenFOAM solver, as shown in Eq.(2). D_i is expressed as

$$D_i = \theta_i \sqrt{\frac{g}{h}} (n+1) \left(\frac{x-x_0}{l} \right)^n \tag{15}$$

where l is the length of the damping zone, x_0 is the distance from the origin to the starting point of the damping zone. n and θ_i are the damping coefficients, $n = 2$, $\theta_i = 0.6$. Similar methods were used by Dong and Zhan^[16]. For the left damping zone, it is also a wave making region and the velocity in this area is modified by $u_i = u_i^m + D_i' (u_i - u_i^m)$ at the end of each time step. D_i' is written as

$$D_i' = \sqrt{1 - \left(\frac{l-x}{l} \right)^2} \tag{16}$$

In addition, the interface capturing scheme in OpenFOAM for two-phase flow is improved. In the course of using this scheme, it is found that the scheme is indeed easy to use and can capture the surface well except that it is very slow. The time step becomes very small and the computation always takes a long time. The reason for this is the large Courant

number of the air phase in the surface domain. In order to solve this problem, a modified scheme is proposed. In the computational domain, if the region is occupied by the air phase, the velocity and the pressure of this zone are set to zero. This will not alter the numerical results because ρ_w is much larger than ρ_a .

3. Numerical results

3.1 Model validation

Firstly, we investigate the characteristics of the flow field in the numerical wave tank. In the present case, $d = 5.0 \text{ m}$, $T = 4.5 \text{ s}$, $A/d = 0.1$, where T is the wave period. When the calculation becomes stable, the time series of the wave profile at $x = 78.9 \text{ m}$ indicate that the damping schemes presented in the present paper work well, as shown in Fig.3. In addition, the calculated horizontal and vertical velocities at the point $x = 78.9 \text{ m}$ and $y = 0 \text{ m}$ are compared with the theoretical results, which shows a good agreement. It is shown that the two-dimensional wave numerical tank performs well for regular waves.

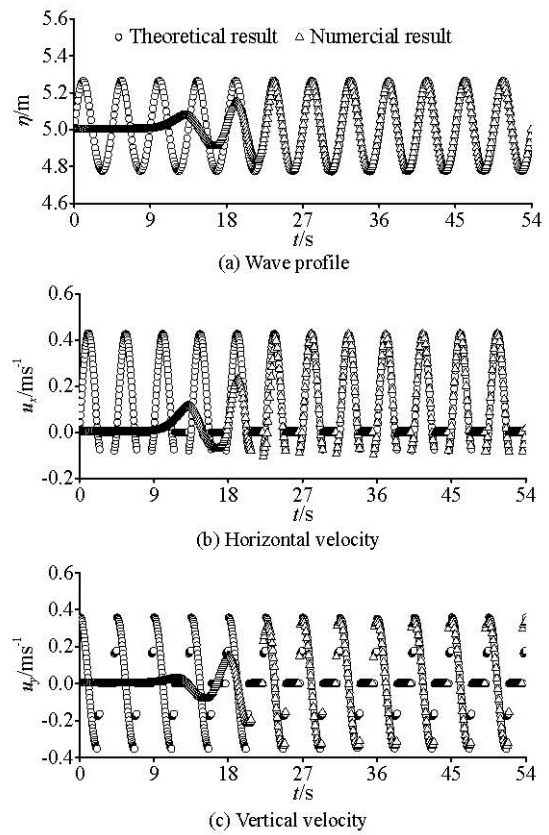


Fig.3 Comparisons of time series for wave profile and velocities

Secondly, for the verification of the simulated

wave forces, the calculation results are compared with Nojiri and Murayama^[11], Maruo^[12], and Koo^[9], respectively. The computational domain is shown in Fig.4, where λ is the wave length. A surface-piercing body is fixed in the middle of the domain and the radius of the round corner is 0.064 m. The input wave properties are listed in Table 1. The incident wave height is 0.07 m. Figure 5 shows the computational meshes used for the simulations. In order to accurately capture the wave surface and calculate the wave forces, the meshes in surface zones and zones along body are refined.

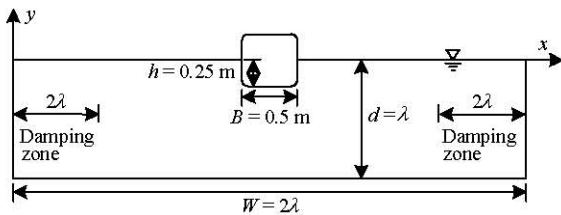


Fig.4 Sketch of the domain for verification

Table 1 Incident wave inputs

Case	ξ	$T\sqrt{g/d}$	A/d	λ (m)
1	0.20	2.50	0.009	7.85
2	0.50	2.50	0.022	3.14
3	0.75	2.50	0.033	2.10
4	1.00	2.50	0.044	1.57
5	1.50	2.50	0.067	1.05
6	1.75	2.50	0.078	0.90

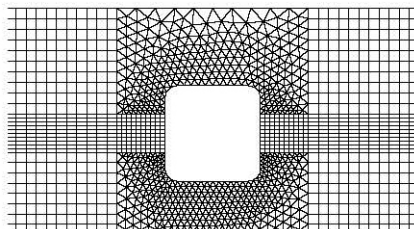


Fig.5 Computational meshes used for the simulation

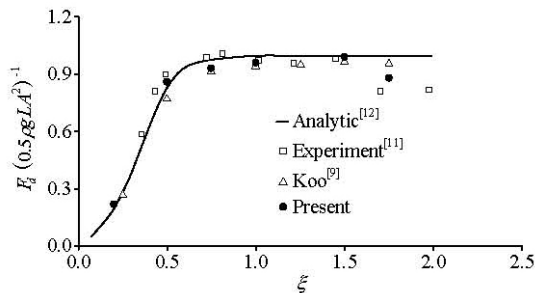


Fig.6 Comparison of drift force

Figure 6 shows the comparison of the drift force with Nojiri’s experimental results, Maruo’s analytical

results and Koo’s numerical results. Figures 7-9 show the comparison of the force components and the moment. The first-harmonic force components and the rotational moment are calculated by Fourier analysis. The computational results are shown to be in good agreement with experimental results except in the region of $\xi > 1.5$. It is believed that the deviation may be attributed to viscous and other nonlinear effects. It is also noted that the present results are more consistent with experimental results than Koo’s, which is based on potential theory. It is shown that the turbulence of fluid has an influence on the wave-body interactions even in deep water.

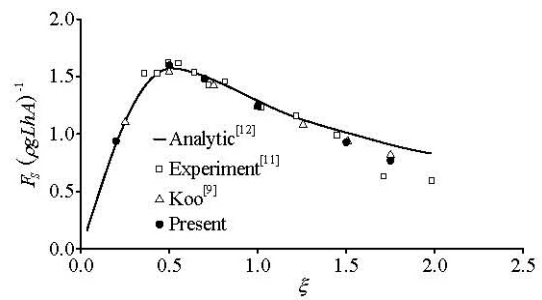


Fig.7 Comparison of first-harmonic horizontal normalized force

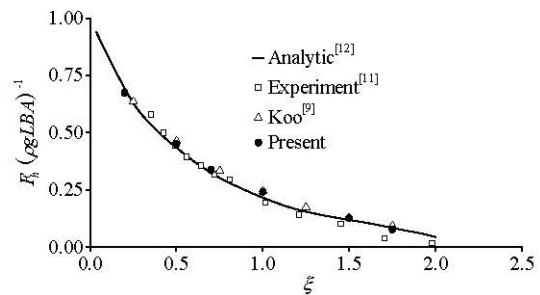


Fig.8 Comparison of first-harmonic vertical normalized force

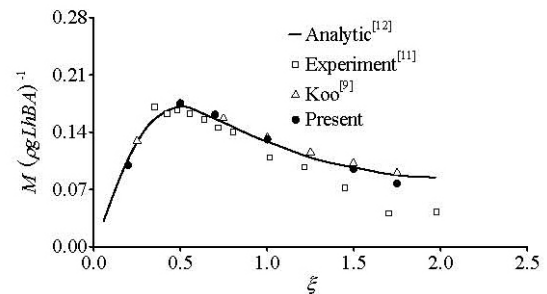


Fig.9 Comparison of first-harmonic normalized moment

3.2 Domain with flat bottom topography

The computational domain is shown in Fig.2 with $\tan \phi = 0$. The length of damping zone is $2\lambda_m$, where λ_m represents the maximum wavelength of all

cases. The water depth for the incident region is 5.0 m. Tables 2 and 3 give, respectively, the values of dimension parameters and the input wave properties, where $T\sqrt{g/d}$ is the dimensionless parameter to represent the nonlinearity of the incident wave.

Table 2 Dimension parameters

W (m)	100
d (m)	5.0
h (m)	0.5
B (m)	5.0

Table 3 Incident wave inputs

Case	ξ	$T\sqrt{g/d}$	A/d	λ (m)
1	0.24	9.1	0.10	41.9
2	0.28	8.4	0.10	38.1
3	0.33	7.7	0.10	34.2
4	0.40	7.0	0.10	30.3
5	0.50	6.5	0.10	26.3
6	0.63	5.6	0.04	22.2
7	0.82	4.9	0.04	18.0
8	1.12	4.2	0.04	13.7
9	1.61	3.5	0.04	9.70

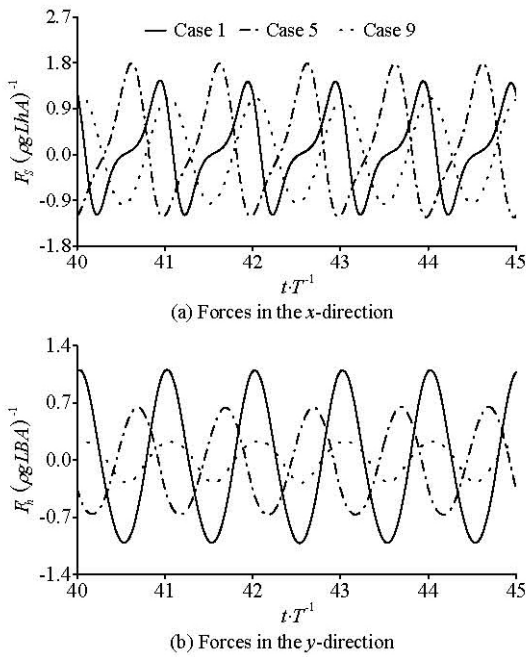


Fig.10 The total forces in the x - and y -directions

Figure 10 shows the total normalized forces (F_x and F_y), which are plotted against the nondimensional time (t/T). In this figure, the steady-state time series results for three different cases are shown, from which a series of harmonic components for horizontal force, vertical force and rotational moment can be obtained. We can also see that the horizontal force shows more nonlinear

features with the increase of $T\sqrt{g/d}$.

Figure 11 shows the comparison of horizontal force components for finite depth and deep water conditions. Horizontal force components for finite water depth condition are approximately similar to the cases for deep water condition, while the first and second order forces are much greater than those in deep water when the wave frequency is low ($\xi < 0.82$). The magnitude of the first order can be 47% greater than that of deep water at $\xi = 0.33$.

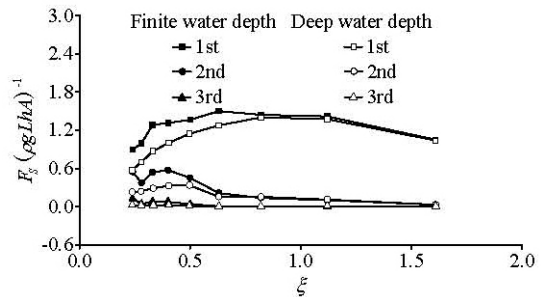


Fig.11 Comparison of horizontal force components for two water depth conditions

The same kind of comparisons for vertical force is shown in Fig.12. The first order vertical force under finite water depth condition is more sensitive to the variations of ξ and is significantly larger than that under deep water condition in four cases with $\xi = 0.24, 0.33, 0.4$ and 0.63 . In case of $\xi = 0.63$, the first-harmonic component can be as large as 25% of that in deep water. Due to the wave reflection from flat bottom and re-reflection from body surface, the first order components can be enhanced.

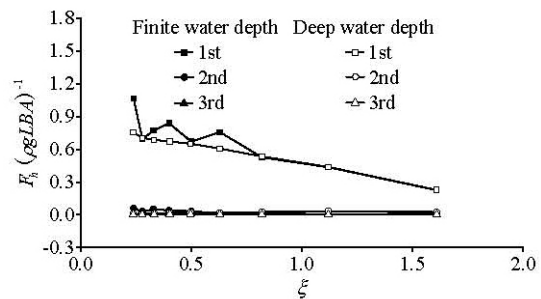


Fig.12 Comparison of vertical force components for two water depth conditions

Figure 13 shows the comparison of rotational moment components for two water depth conditions. The first order component under finite water depth condition is much greater than that under deep water condition for cases with low frequencies ($\xi < 0.82$). Specially, the magnitude of the first order component gradually increases up to 144% of the value at the

case of $\xi = 0.33$. This phenomenon indicates that the state of the structure becomes more unstable and precarious in shallow water than in deep water, especially when the frequency is low.

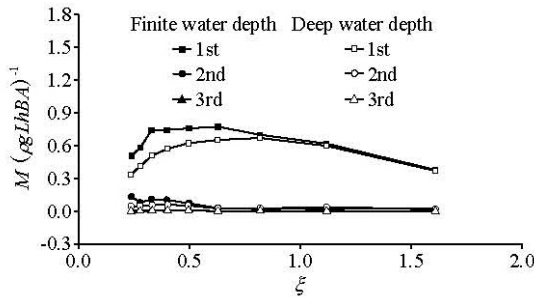


Fig.13 Comparison of moment components for two water depth conditions

3.3 Domain with sloping bottom topography

The computational domain is shown in Fig.2 with $\tan\phi = 0.03$. Computational conditions and input settings for sloping bottom topography are the same as those for flat bottom topography.

Figures 14-16 show the comparison of horizontal force, vertical force and rotational moment components for sloping bottom and flat bottom topography. Because of the wave reflection from sloping bottom, not only the vertical force component but also the horizontal force and rotational moment components are affected. The first order components become much larger in some cases.

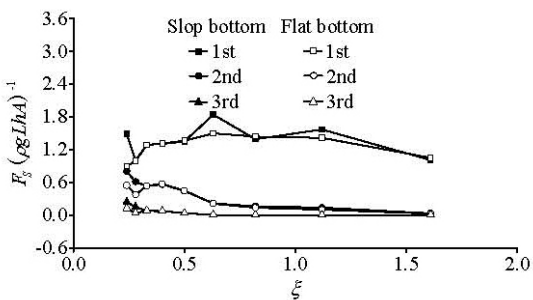


Fig.14 Comparison of horizontal force components for two types of bottom topographies

As for the horizontal force component, the values for two types of bottoms are almost the same for ξ in the range between 0.28 and 0.5, while the first-harmonic component is 23% greater than that for flat bottom in case of $\xi = 0.63$. A similar trend for the variations of the moment component can be observed in Fig.16.

From Fig.15, we can see that the first order vertical force for sloping bottom is larger than that for flat bottom when $\xi > 0.71$. The second and third

order components of all parameters for sloping bottom condition are close to the results for flat bottom condition except in the low frequency region ($\xi < 0.33$).

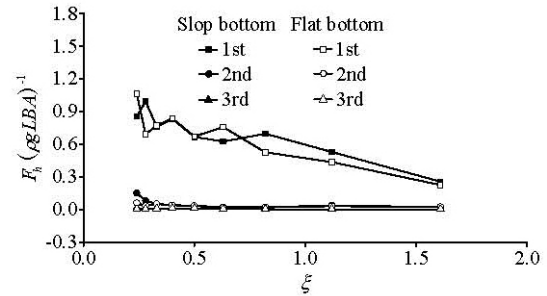


Fig.15 Comparison of vertical force components for two types of bottom topographies

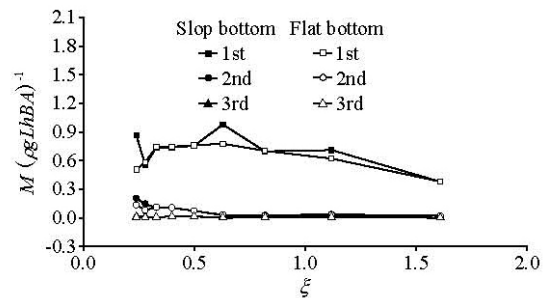


Fig.16 Comparison of moment components for two types of bottom topographies

4. Conclusions

In the present article, the nonlinear wave-body interactions for a stationary surface-piercing body under regular waves in water of finite depth are simulated in a 2-D numerical wave tank. The tank model is based on Reynolds averaged Navier–Stokes equations and $k-\epsilon$ two-equation model. The central difference scheme and QUICK scheme are employed to represent the diffusion term and convection term, respectively. The PCG method is employed for solving the algebraic equations. Boundary conditions associated with regular waves are prescribed along the left side of the computational domain. Accordingly, artificial damping zones are allocated at the two ends of the domain to absorb the wave energy reflection and re-reflection. In order to capture the water-air free surface, VOF method and CICSAM scheme are adopted. All these features are implemented by utilizing the open source code named OpenFOAM.

In the solution of the fluid domain, the time history of the wave nonlinear force on the bodies can be obtained by integrating the pressure and viscous force. By using the force time histories, the mean and

higher-harmonic force components are calculated. Under the finite water depth condition, the first order forces and rotational moment components are much greater than those under deep water condition when the frequency is low. For the domain with sloping bottom topography, the second and third order components of all parameters under sloping bottom conditions are close to the results under flat bottom condition except in the low frequency region. Due to the wave reflection and re-reflection, the forces and rotational moment components vary in a complicated way with the increase of frequency ξ , especially under the sloping bottom condition.

References

- [1] KOO W. C., KIM M. H. and TAVASSOLI A. Fully nonlinear wave-body interactions with fully submerged dual cylinders[J]. **International Journal of Offshore and Polar Engineering**, 2004, 14(3): 210-217.
- [2] VENGATESAN V., VARYANI K. S. and BARLTROP N. D. P. Wave force coefficients for horizontally submerged rectangular cylinders[J]. **Ocean Engineering**, 2006, 33(11-12): 1669-1704.
- [3] LIU Yong, LI Yu-cheng and TENG Bin. Wave motion over two submerged layers of horizontal thick plates[J]. **Journal of Hydrodynamics**, 2009, 21(4): 453-462.
- [4] SUNG H. G., HONG S. Y. and CHOI H. S. Evaluation of nonlinear wave forces on a fixed body by numerical wave tank techniques[C]. **Proceedings of the 3rd International Conference on Hydrodynamics**. Seoul, Korea, 1998, 191-196.
- [5] LI Chi-wai, LIN Peng-zhi. A numerical study of three-dimensional wave interaction with a square cylinder[J]. **Ocean Engineering**, 2001, 28(12): 1545-1555.
- [6] YOU Yun-xiang, SHI Qiang and MIAO Guo-ping. The radiation and diffraction of water waves by a bottom-mounted circular cylinder in a two-layer fluid[J]. **Journal of Hydrodynamics, Ser. B**, 2007, 19(1): 1-8.
- [7] TANIZAWA K., MINAMI M. Estimation of wave drift force by numerical wave tank[C]. **Proceedings of the 9th ISOPE Conference**. Brest, France, 1999, 69-75.
- [8] BAI Wei, TENG Bin and QIU Da-hong. Real time simulation of second-order radiation of 3D bodies[J]. **Journal of Hydrodynamics, Ser. A**, 2003, 18(4): 489-498(in Chinese).
- [9] KOO W. C., KIM M. H. Fully nonlinear wave-body interactions with surface-piercing bodies[J]. **Ocean Engineering**, 2007, 34(7): 1000-1012.
- [10] WANG Da-guo, ZOU Zhi-li and TANG Chun-an. Time stepping solutions of nonlinear wave forces on a three-dimensional box-shaped ship in a harbor[J]. **Journal of Ship Mechanics**, 2007, 11(4): 533-544(in Chinese).
- [11] NOJIRI N., MURAYAMA K. A study on the drift force on two dimensional floating body in regular waves[J]. **Transactions of the West-Japan Society Naval Architect**, 1975, 51: 131-152.
- [12] MARUO H. On the increase of the resistance of a ship in rough seas[J]. **Journal of Zosen Kiokai**, 1960, (108): 5-13(in Japanese).
- [13] UBBINK O., ISSA R. I. A method for capturing sharp fluid interfaces on arbitrary meshes[J]. **Journal of Computational Physics**, 1999, 153(1): 26-50.
- [14] QI Peng, WANG Yong-xue and HOU Yi-jun. Numerical simulation of solitary waves overtopping a breakwater[J]. **Journal of Hydrodynamics, Ser. A**, 2004, 19(12): 884-889(in Chinese).
- [15] XU Shao-kun. A numerical wave tank based on OpenFOAM and its application[D]. Ph. D. Thesis, Tianjin: Tianjin University, 2008(in Chinese).
- [16] DONG Zhi, ZHAN Jie-min. Comparison of existing methods for wave generating and absorbing in VOF-based numerical tank[J]. **Journal of Hydrodynamics, Ser. A**, 2009, 24(1): 15-21(in Chinese).